



Research papers

Eddy-induced transport of the Kuroshio warm water around the Ryukyu Islands in the East China Sea

Yuki Kamidaira^{a,*}, Yusuke Uchiyama^b, Satoshi Mitarai^c^a Nuclear Science and Engineering Center, Japan Atomic Energy Agency, Tokai, Ibaraki, Japan^b Department of Civil Engineering, Kobe University, Kobe, Hyogo, Japan^c Marine Biology Unit, Okinawa Institute of Science and Technology, Onna, Okinawa, Japan

ARTICLE INFO

Keywords:

Submesoscale eddy
Kuroshio
Topography
East China Sea
ROMS

ABSTRACT

In this study, an oceanic downscaling model in a double-nested configuration was used to investigate the role played by the Kuroshio warm current in preserving and maintaining biological diversity in the coral coasts around the Ryukyu Islands (Japan). A comparison of the modeled data demonstrated that the innermost submesoscale eddy-resolving model successfully reproduced the synoptic and mesoscale oceanic structures even without data assimilation. The Kuroshio flows on the shelf break of the East China Sea approximately 150–200 km from the islands; therefore, eddy-induced transient processes are essential to the lateral transport of material within the strip between the Kuroshio and the islands. The model indicated an evident predominance of submesoscale anticyclonic eddies over cyclonic eddies near the surface of this strip. An energy conversion analysis relevant to the eddy-generation mechanisms revealed that a combination of both the shear instability due to the Kuroshio and the topography and baroclinic instability around the Kuroshio front jointly provoke these near-surface anticyclonic eddies, as well as the subsurface cyclonic eddies that are shed around the shelf break. Both surface and subsurface eddies fit within the submesoscale, and they are energized more as the grid resolution of the model is increased. An eddy heat flux (EHF) analysis was performed with decomposition into the divergent (dEHF) and rotational (rEHF) components. The rEHF vectors appeared along the temperature variance contours by following the Kuroshio, whereas the dEHF properly measured the transverse transport normal to the Kuroshio's path. The diagnostic EHF analysis demonstrated that an asymmetric dEHF occurs within the surface mixed layer, which promotes eastward transport toward the islands. Conversely, below the mixed layer, a negative dEHF tongue is formed that promotes the subsurface westward warm water transport.

1. Introduction

Coral reefs are home to the most diverse range of marine life in the world. They are of great importance to marine ecosystems, hosting favorable habitat to a wide variety of flora and fauna. An estimated 25% of all marine life is supported by coral reefs, even though they cover < 0.1% of the world's oceans and represent one of the most fragile and endangered marine ecosystems in the world (e.g., Spalding et al., 2001). Coral reefs also represent a vital resource for humankind in terms of tourism and fishing. Cesar et al. (2003) reported that coral reefs provide approximately US\$29.8 billion in net benefit streams per annum in goods and services to world economies, including tourism (US\$9.6 billion), fisheries (US\$5.7 billion), and coastal protection (US\$9.0 billion). Similarly, coral reefs have great economic value in Japan, generating as much as US\$1.6 billion per annum domestically. In particular, the Ryukyu Islands, located in the subtropical region of

Japan that fringes the East China Sea (ECS; Fig. 1), have ecologically abundant coral reefs situated at their northernmost end at the border between the Pacific and Indian oceans. These corals lie within a region that supports the highest diversity of indigenous species in the world.

Water temperature is widely known as a factor that has considerable effect on coral growth. The ideal range of ambient temperature for reef corals is narrow; most corals cannot survive in temperatures much below 16–18 °C even for a few weeks. High temperatures also have a serious effect on coral growth and can lead to “coral bleaching,” a process that results in devastating mass mortality of the coral during which they expel their symbiotic algae. Therefore, the habitat of coral is generally restricted to a latitudinal band between 30°N and 30°S because decreasing temperature follows increasing latitude.

The sea around the Ryukyu Islands in the ECS, located between 25°N and 30°N, provides an environment for coral growth even though it lies at the northernmost extreme of the habitable region. Major warm

* Corresponding author.

E-mail addresses: kamidaira.yuki@jaea.go.jp (Y. Kamidaira), uchiuyama@harbor.kobe-u.ac.jp (Y. Uchiyama), satoshi@oist.ac.jp (S. Mitarai).

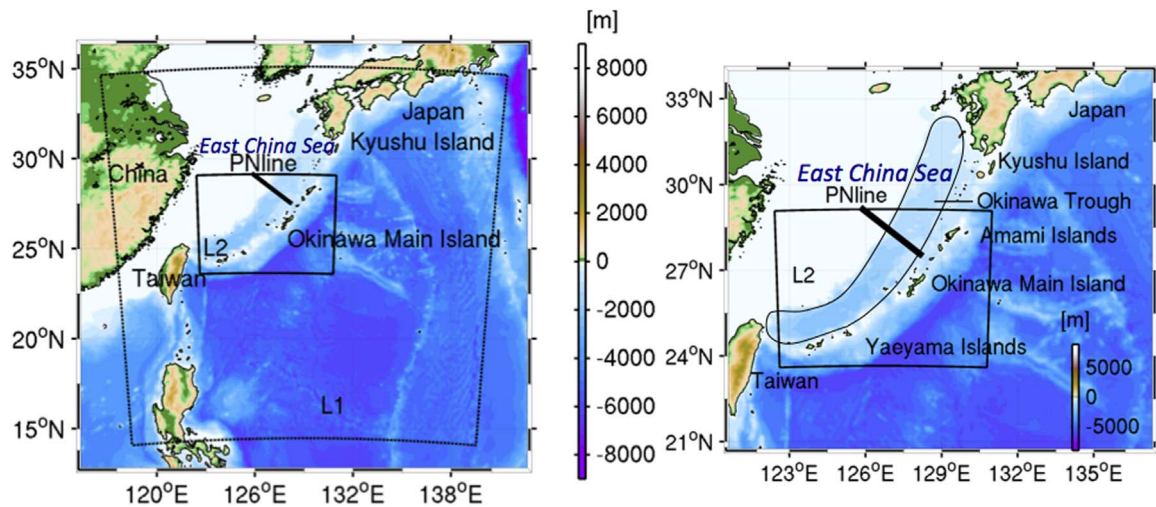


Fig. 1. Double-nested ROMS model domains and bathymetry (color: m). Left: the ROMS-L1 and L2 domains embedded in the JCOPE2 domain. Right: a zoomed-in region of the ROMS-L2 domain. Black thick line indicates the JMA PN Line transect.

Table 1

Computational configurations for the ROMS-L1 and ROMS-L2 models.

Models	L1	L2
Computational period	1/1/2005-9/14/2013	12/27/2010-9/14/2013
Grid cells	768 × 768 (×32 layers)	832 × 608 (×32 layers)
Horizontal grid resolution	3.0 km	1.0 km
Baroclinic time step	240 sec	60 sec
Surface wind stress	QuikSCAT-ECMWF (daily, till 12/31/2007) JMA GPV-GSM (daily, 1/1/2008 and later)	JMA GPV-MSM (hourly)
Surface flux	COADS (monthly climatology)	
SST and SSS to restore	JCOPE2 (20-day averaged)	
Major river discharges (Yangtze River)	monthly climatology	—
Boundary/Initial condition	JCOPE2 (daily)	ROMS-L1 (daily)
TS nudging	JCOPE2 (10-day averaged)	—
Topography	SIO SRTM30_Plus	

currents, such as the Kuroshio, allow the development of reefs up to and beyond the ordinary habitable latitudinal limit. These ocean currents play important roles in transporting coral larvae and warm water to such areas, thus maintaining favorable environments for reef corals.

The Kuroshio, which is one of the world's major western boundary

currents of the North Pacific subtropical gyre, enters the ECS from the east coast of Taiwan. It turns northeastward and drifts along the continental shelf slope fringing the ECS around the Ryukyu Islands (Qiu, 2001). The Kuroshio not only plays an essential role in the meridional transport of large amounts of warm and salty tropical water northward (e.g., Ichikawa and Beardsley, 1993; Ichikawa and Chaen, 2000; Imawaki et al., 2001; Johns et al., 2001; Andres et al., 2008; Yang et al., 2011) but also influences the regional climatic system of the ECS (e.g., Xu et al., 2011; Sasaki et al., 2012). Temperature measurements recorded continuously by more than 100 thermometers in conjunction with satellite SST (sea surface temperature) measurements have revealed that areas of high SST are formed off the middle of the west coast of Okinawa Island because of the Kuroshio warm water (Nadaoka et al., 2001).

Several numerical studies have been undertaken to investigate the physical processes and effects of the Kuroshio in the ECS. Guo et al. (2003) were successfully demonstrated that the path and vertical structure of the Kuroshio in the ECS are reproduced more realistically as the horizontal resolution of a model increases on the basis of a triply nested ocean modeling using the Princeton Ocean Model (Blumberg and Mellor, 1987). Based on a study using the Meteorological Research Institute Community Ocean Model (Usui et al., 2006), Usui et al. (2008) reported that frontal waves are generated as a result of the collisions between anticyclonic mesoscale eddies with diameters at orders of 100 km. These eddies are considered to have nontrivial influence on mass and heat transport between the Kuroshio and the Ryukyu Islands. Their study suggested that eddy-induced lateral mixing must be substantial to promote the warm water intrusion

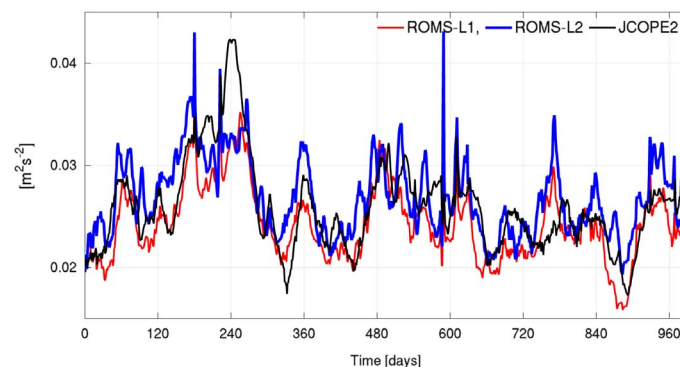


Fig. 2. Time series of the volume-averaged surface ($z > -400$ m) kinetic energy from the ROMS-L1 (red), ROMS-L2 (blue), and JCOPE2 (black) models. The abscissa indicates the elapsed time in days since December 27, 2010, UTC. (For interpretation of the references to color in this figure legend, the reader is referred to the web version of this article.)

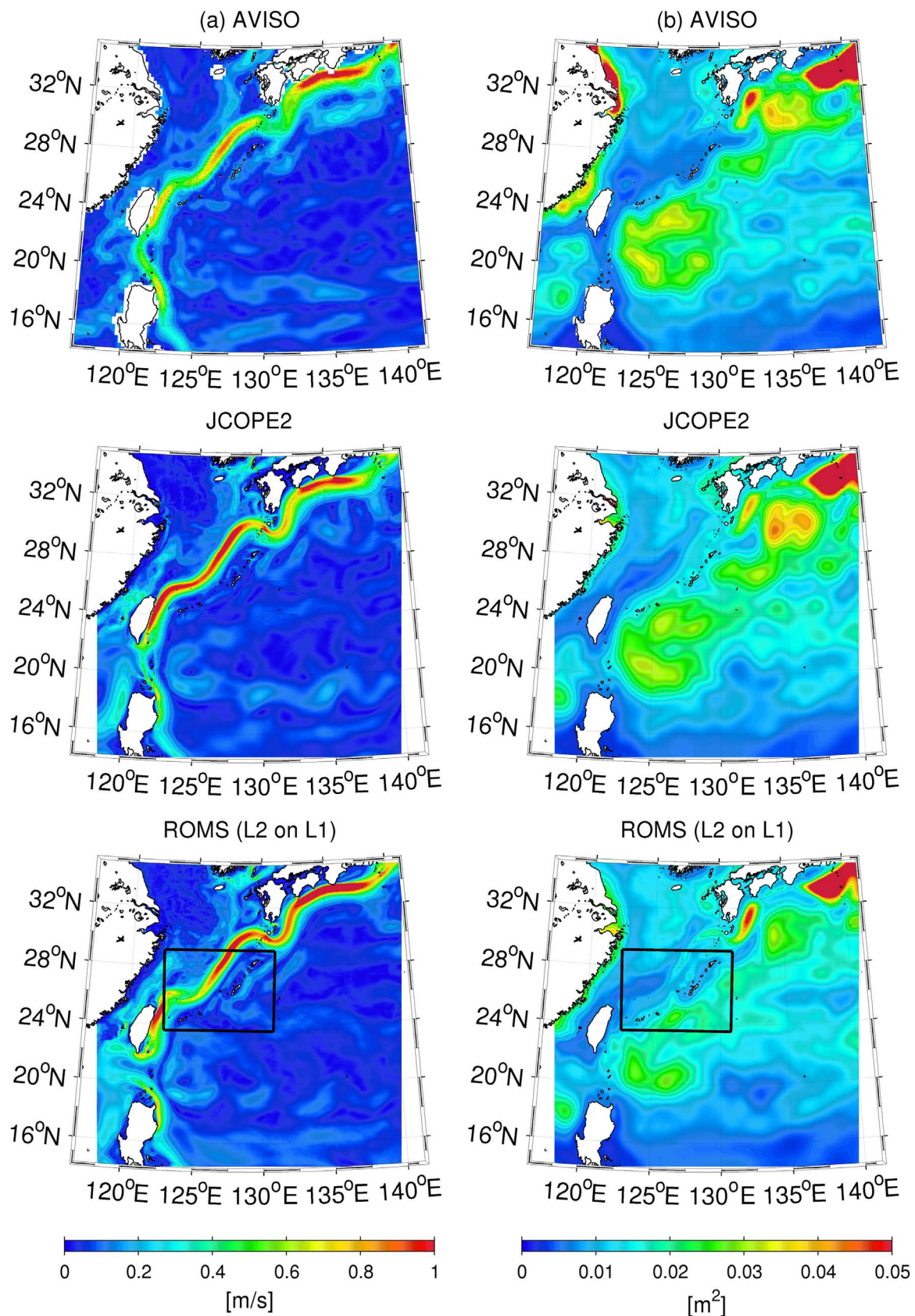


Fig. 3. Plan view plots of: (a) time-averaged surface velocity magnitude and (b) SSH variance. Top: AVISO data, middle: JCOPE2, and bottom: ROMS-L2 on L1.

toward the Ryukyu Islands, because the main body of the Kuroshio is persistently located approximately 150–200 km to the west of the islands, restricting its direct impact.

Recently, the effects of submesoscale eddies (at typical horizontal scales of several to tens of km or less) on the mean oceanic structure, stratification, and frontal processes have been studied actively to

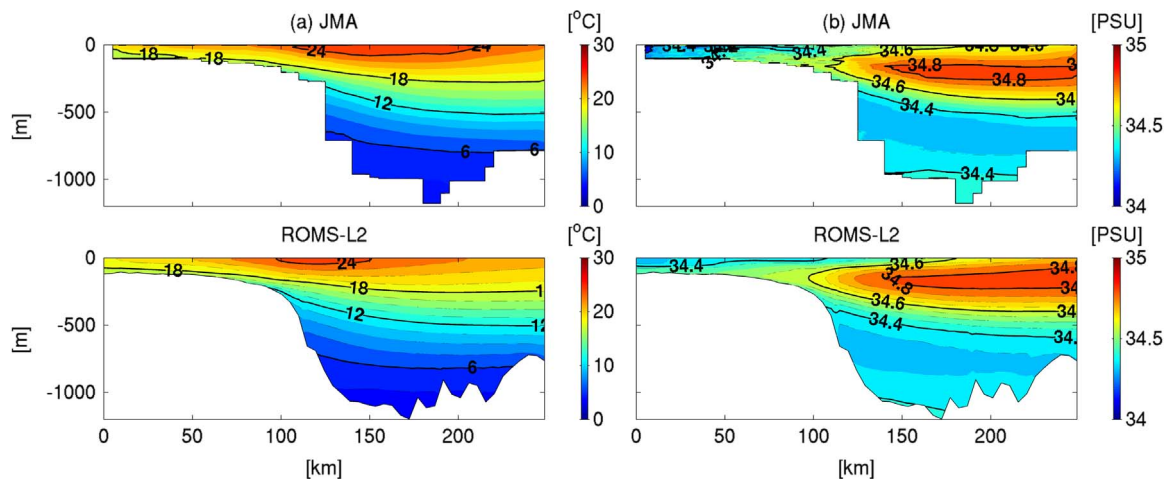


Fig. 4. Seasonally averaged temperature (left) and salinity (right) for spring from JMA observations (upper panels) and ROMS-L2 (lower panels) in the vertical section along the PN Line.

Table 2

Seasonally averaged volume flux in Sverdrup across the PN Line from the *in situ* observations, JCOPE2, ROMS-L1, and ROMS-L2 models.

	Spring	Summer	Fall	Winter
observation	26.4	26.9	25.1	26.0
JCOPE2	30.0	32.9	31.4	31.0
ROMS-L1	27.8	29.5	27.4	29.2
ROMS-L2	27.9	29.2	27.3	28.0

enhance our understanding of the dynamic processes of the upper oceans (e.g., Boccaletti et al., 2007; Badin et al., 2011; Callies et al., 2015; Kunze et al., 2015). Capet et al. (2008a, 2008b, 2008c) conducted a high-resolution numerical experiment of the idealized California Current System using the Regional Oceanic Modeling System (ROMS; Shchepetkin and McWilliams, 2005, 2008). They demonstrated that submesoscale eddies occur through frontogenesis, which sharpens the surface density fronts, forming in the regions of high strain on the flanks of mesoscale eddies, down to horizontal scales of a few kilometers or less in association with strong vertical ageostrophic secondary circulations in the surface boundary layer. A multiple nesting technique (e.g., Marchesiello et al., 2003; Penven et al., 2006; Mason et al., 2010) has enabled submesoscale eddy-resolving ocean modeling to investigate submesoscale stirring and mixing in the upper oceans and associated material dispersal. For example, Romero et al. (2013) conducted a Lagrangian particle tracking in the Santa Barbara Channel, CA, USA, using quadruple-nested high-resolution ROMS modeling with a 75-m horizontal grid size. Uchiyama et al. (2014) performed a Eulerian passive tracer tracking for sewage outfalls in the Santa Monica and San Pedro bays in the Southern California Bight using a similar quadruple-nested downscaling ocean modeling. Both studies exhibited anisotropic along- and cross-shelf dispersal of material concentrations and particles on the continental shelves and nearshore areas, markedly dominated by submesoscale-eddy mixing. In addition to those studies focusing on the eastern boundary currents, several other studies have investigated the western boundary currents, such as the Kuroshio and its extension region off Japan (e.g., Sasaki et al., 2014) and the Gulf Stream off the U. S. east coast (e.g., Gula et al., 2014). However, the influence of submesoscale eddies on upper-ocean dynamics and the resultant dispersal and transport of materials, including the Kuroshio-derived warm water, nutrients, and coral larvae, has not yet been investigated adequately around the Ryukyu Islands in the ECS.

Another important aspect of the Ryukyu Islands is their upheaved shallow topography on the relatively deep Ryukyu Trough, which is

situated on the eastern side of the ECS continental shelf break where the Kuroshio persistently flows northeastward. The islands obstruct the westward-propagating mesoscale eddies that detach from the Kuroshio recirculation (Nakamura et al., 2009). Therefore, this obstruction may result in the emergence of unique turbulence such as island wakes and associated eddy shedding, as has been investigated in the Southern California Bight (e.g., Dong and McWilliams, 2007). These geographical configurations are presumed to set preferable conditions for the development of submesoscale-eddy mixing through baroclinic and barotropic instability due to the Kuroshio fronts and topographic shear within the study area.

In the present study, a submesoscale-eddy-resolving numerical experiment was conducted for the area around the Ryukyu Islands. The study was based on a double-nested ocean downscaling configuration using the ROMS, embedded in the assimilative Japan Coastal Ocean Predictability Experiments (JCOPE2) oceanic reanalysis (Miyazawa et al., 2009) with atmospheric forcing from the assimilative GPV-GSM (e.g., Roads, 2004) and MSM (e.g., Isoguchi et al., 2010) reanalysis products. The innermost ROMS model domain (the principal focus of this analysis) had 1-km horizontal grid spacing, which was suitably fine for full representation of submesoscale activities (Capet et al., 2008a, 2008b). Particular attention was given to the model's reproducibility, statistical description of intrinsic submesoscale eddies, possible mechanisms for eddy inducement, and influence of the eddies on the lateral mixing that promotes transport of the Kuroshio water toward the islands. The remainder of this paper is organized as follows. A description of the modeling framework used for the hindcast experiment for the years 2010–2013 is given in Section 2. Section 3 illustrates an extensive comparison between the model results and field observation and satellite altimetry data in order to validate the model's capability of reproducing the Kuroshio and 3-D oceanic structure. Section 4 considers the impact of downscaling, which is followed by analyses of both the energy conversion and instability relevant to eddy kinetic energy in Section 5 and of the heat flux in Section 6. Conclusions are given in Section 7.

2. Model configuration

Fig. 1 shows the numerical domains of the oceanic downscaling model in a double-nested configuration embedded in the JCOPE2 (Miyazawa et al., 2009) domain. The JCOPE2 is a numerical reanalysis product for the northwestern Pacific Ocean assimilated with a vast amount of satellite and *in situ* data, including ARGO floats using 3D-VAR. The JCOPE2 product is provided as daily averaged sea surface height (SSH), temperature, salinity, and meridional and zonal hor-

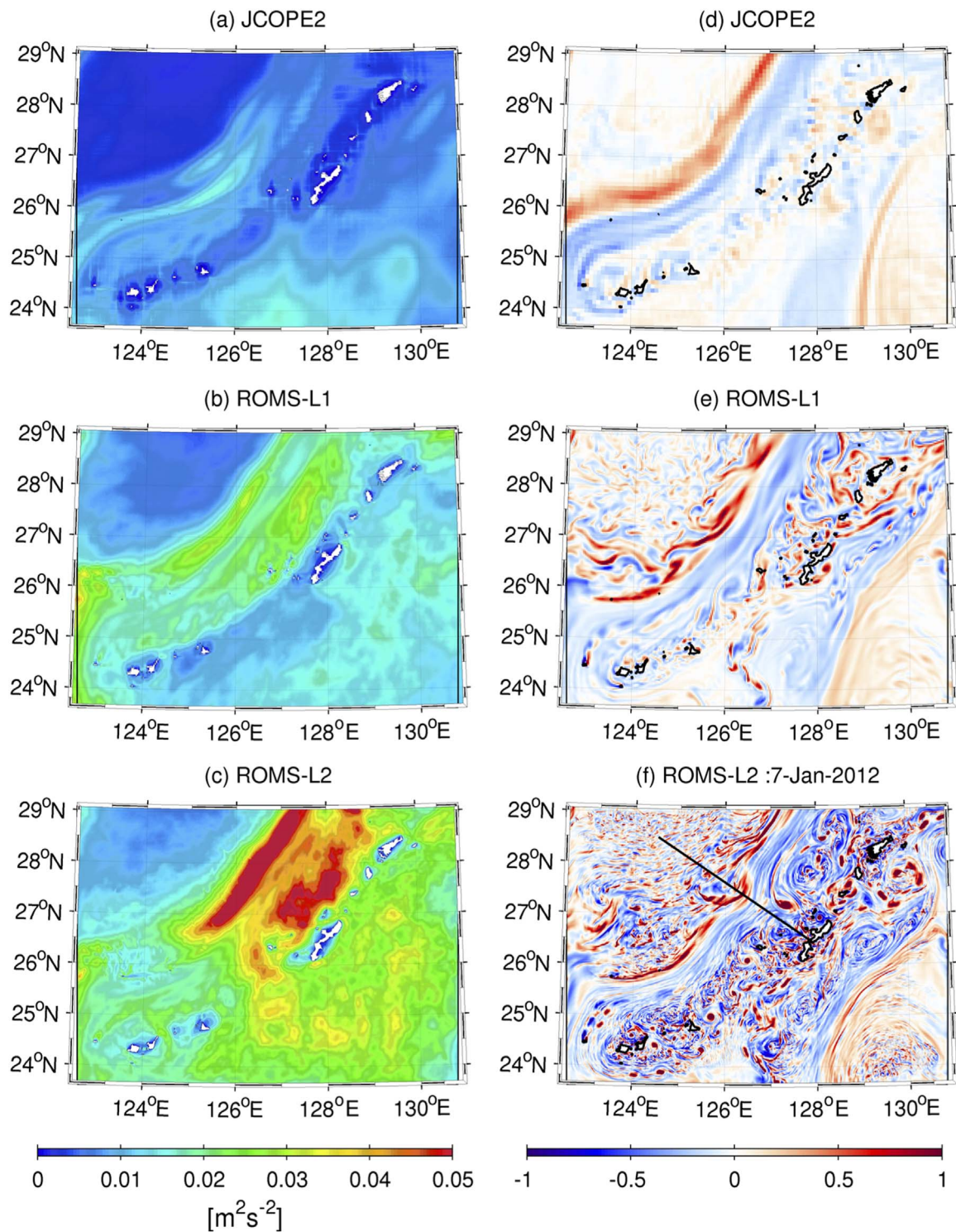


Fig. 5. Left panels—surface eddy kinetic energy (EKE), K_e , from: (a) JCOPE2, (b) ROMS-L1, and (c) ROMS-L2. Right panels—instantaneous spatial distributions of surface vorticity normalized by planetary vorticity, ζ/f (dimensionless) on January 7, 2012 from: (d) JCOPE2, (e) ROMS-L1, and (f) ROMS-L2. The black line in (f) indicates transect AA' for the cross-sectional plots.

horizontal current velocities. We relied on a one-way offline nesting approach (Mason et al., 2010) to reduce the horizontal grid size from approximately 10 (JCOPE2) to 3 km (ROMS-L1), and ultimately, down to 1 km (ROMS-L2). The parent ROMS domain (ROMS-L1) had a horizontal size of 2304×2304 km with uniformly square 3-km grid spacing and vertically stretched 32 s -layers, designed to encompass a wide area to consider all possible impacts of the Kuroshio flowing in from the Taiwan Strait and the Luzon Strait. The climatological

monthly freshwater discharge of the Yangtze River into the ECS, which is reported to range approximately between 838–907 km^3/yr (e.g., Dai et al., 2009), was taken into account. The innermost ROMS-L2 domain was 832×608 km with 1-km horizontal resolution and 32 vertical s -layers, which covered the entire chain of the Ryukyu Islands, from the Amami Islands of Kagoshima Prefecture in the north to the Yaeyama Islands of Okinawa Prefecture in the south. Table 1 lists the numerical configuration of the ROMS models.

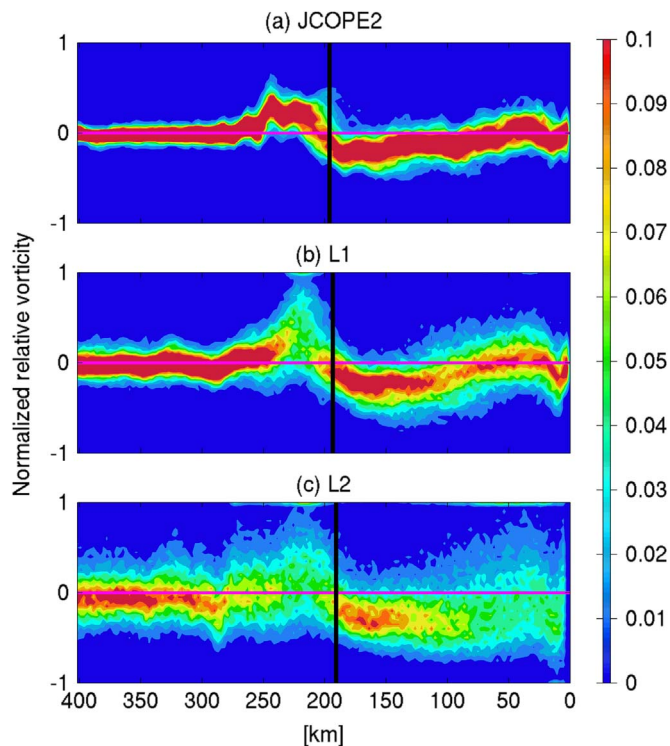


Fig. 6. Probability density functions of the normalized relative vorticity at 2 m depth along transect AA' (see Fig. 5f) from: (a) JCOPE2, (b) ROMS-L1, and (c) ROMS-L2 models, as a function of distance from Okinawa Island (km). The black lines are the mean Kuroshio axes.

The outermost boundary and initial conditions of ROMS-L1 were obtained from the spatiotemporally interpolated fields of the daily averaged JCOPE2 data. The model topography was obtained from the SRTM 30 Plus product (SRTM: Shuttle Radar Topography Mission; Rodriguez et al., 2005; Becker et al., 2009), which covers the global ocean at 30 geographic arc seconds, or roughly 1 km. We utilized the QuikSCAT-ECMWF blended wind (e.g., Bentamy et al., 2006) for 2005–2007 and the JMA GPV-GSM product (JMA: Japan Meteorological Agency, GPV-GSM: grid point value of the Global Spectral Model) with horizontal resolution of $0.2^\circ \times 0.25^\circ$ for 2008–2013 for surface momentum forcing, depending on the availability of these data sets. Surface heat, freshwater and radiation fluxes were taken from the COADS (Comprehensive Ocean–Atmosphere Data Set; Woodruff et al., 1987) monthly climatology. The 20-day averaged JCOPE2 data were applied to the SST and sea surface salinity (SSS) restoration with a time scale of 90 days to correct long-term biases caused by the imposed climatological surface fluxes. The monthly climatology of the major river discharges in Dai et al. (2009) was applied for the Yangtze River. A four-dimensional TS nudging (a.k.a. robust diagnostic; e.g., Marchesiello et al., 2003) with a weak nudging time scale of 1/20 per day was applied to the 10-day averaged JCOPE2 temperature and salinity fields for consistency of the Kuroshio path reproduced by the ROMS-L1 with that of JCOPE2. The L1 model was used for more than eight years from January 1, 2005 until September 14, 2013, UTC.

The innermost L2 model was initialized and forced along the boundary perimeters by the spatiotemporally interpolated daily averaged L1 output. The hourly output of the JMA GPV-MSM (Mesoscale Model) reanalysis, which encompasses the entire L2 domain with horizontal resolution of $0.05^\circ \times 0.0625^\circ$, was used for the L2 model instead of the GPV-GSM. Similar to the L1 model, SST and SSS restoration for surface flux correction was included. The other numerical conditions were the same as for the L1 model. Hence, the L2 model was run freely without any assimilation such as the TS nudging that

could interfere with the spontaneous development and decay of intrinsic eddies. We note that the present model does not include tidal forcing since it is considered to have minor effects on mean and eddy field in such an open ocean configuration. For instance, Romero et al. (2013) pointed out that dispersal and mixing in Santa Barbara Channel, CA, USA, are dominated much prominently by submesoscale stirring, not by tides. The L2 model computational period was approximately 33 months, from December 27, 2010 to September 14, 2013, UTC. The statistical analyses conducted in the present study exploit the model results for the same period between March 27, 2011 and September 14, 2013, unless otherwise noted.

3. Model validation

In this section, we compare the model results with satellite, *in situ* observations, and the assimilative JCOPE2 reanalysis. Fig. 2 shows the time series of the volume-averaged surface kinetic energy (KE) for the three model results (i.e., JCOPE2, ROMS-L1, and ROMS-L2). The volume average is taken over the entire ROMS-L2 domain from the surface to a depth of 400 m, encompassing the region in which the Kuroshio main body is most influential. The temporal variations of the upper-ocean KE in the three models are similar. Given the fact that JCOPE2 is assimilated with multiple satellite altimetry data, SST, ARGO, and *in situ* mooring data, the two ROMS models provide realistic estimates of the near-surface eddy activities. The ROMS-L2 generally yields slightly larger KE than the other cases because it is a submesoscale eddy-resolving model that results in more energetic KE, while retaining adequate seasonal variability. This result is achieved if the L1 model is run with weak TS nudging toward the low-frequency JCOPE2 3-D density field, to dissipate KE appropriately for realistic replication of the Kuroshio's behavior. Otherwise, the KE in the L1 model increases significantly with unrealistically large meandering of the Kuroshio path (not shown). Conversely, the L2 model with the assimilated L1 boundary forcing behaves favorably, as shown in Fig. 2, without any controls such as TS nudging.

Extensive model-data comparisons are performed using satellite altimetry data and JMA observations to demonstrate the reproducibility of the double-nested ROMS model. For validating the mean structure and temporal variance of the surface currents, including the Kuroshio, we exploited the gridded composite of multiple satellite altimetry data provided by AVISO (e.g., Traon et al., 1998). The delayed-time AVISO-SSH data set is available daily with horizontal spacing of $1/4^\circ$. The magnitude of the time-averaged geostrophic current velocity, estimated from the AVISO-SSH, exhibits comparable magnitude with the corresponding patterns of the JCOPE2 and ROMS-L2 on the L1 (Fig. 3). However, the Kuroshio intrusion into the South China Sea from Luzon Strait in the ROMS-L1 model occurs more apparently than that in AVISO and JCOPE2 where the westward meander is weakened with generating a leaped eddy or a ring. The looping in the Luzon Strait could be realistic since it has been reported both observationally and computationally (e.g., Centurioni et al., 2004 and Miyazawa et al., 2004). Nevertheless, Luzon Strait is located sufficiently far from the study area, and thus we conclude the plots of the ROMS velocity magnitude also show reasonable agreement with the Kuroshio path of the other two data sets. The SSH variance is viewed as a proxy that measures the intensity of the temporal variability in synoptic and mesoscale signals mostly due to eddies and the Kuroshio meanders. The ROMS-derived SSH variance reproduces several important features with equivalent magnitudes to the AVISO data. For instance, the variance is smaller on the persistent Kuroshio path on the western side of the Ryukyu Islands, compared with the other side, where the westward-traveling Rossby waves and mesoscale eddies collide with the topographic ridge around the islands. Another energetic area commonly arises north of 29°N , off the southwest coast of Kyushu Island.

The modeled stratification is subsequently compared with *in situ*

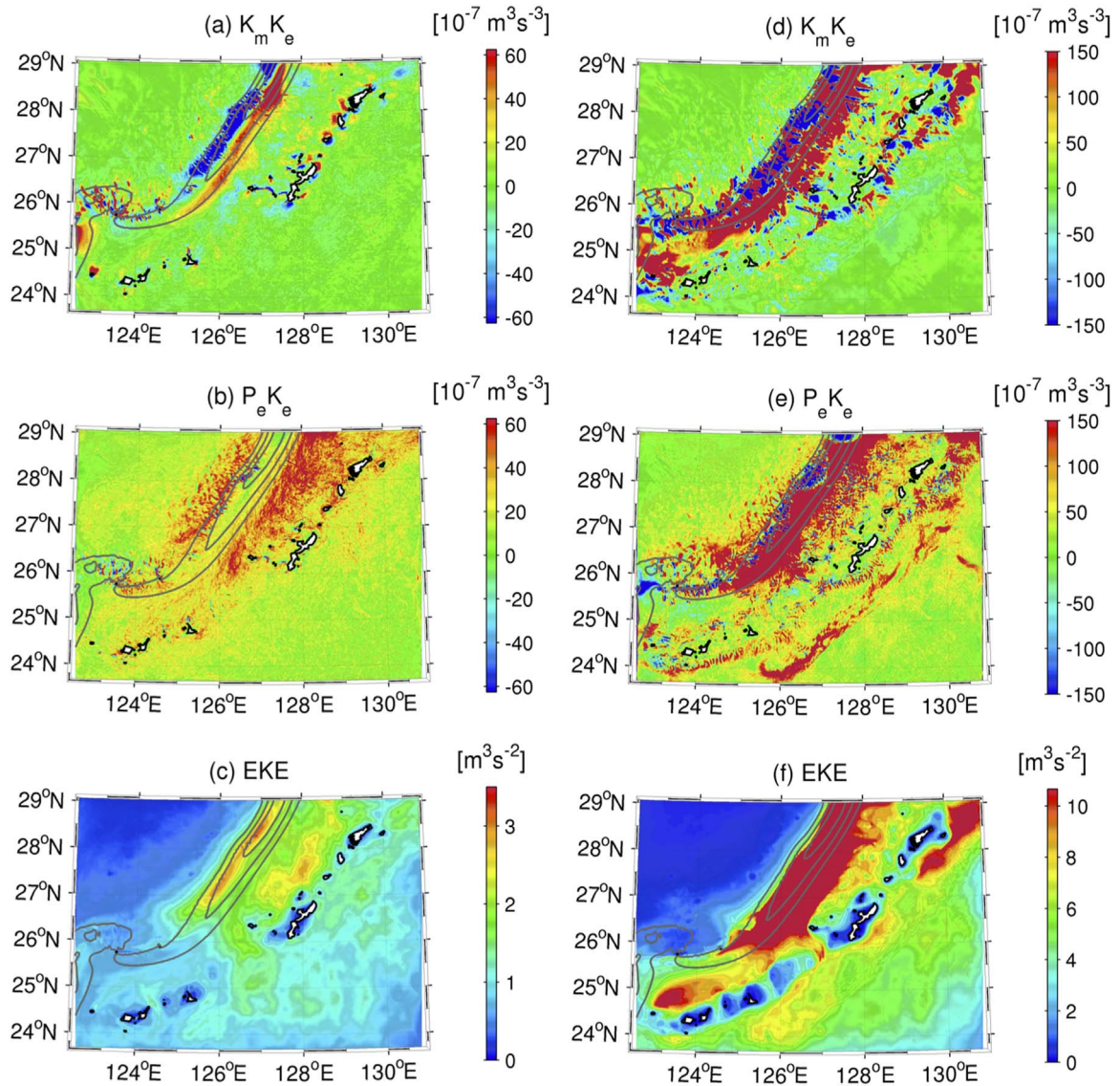


Fig. 7. Left panels: (a) barotropic conversion rate, $K_m K_e$, (b) baroclinic conversion rate, $P_e K_e$, and (c) EKE, K_e , integrated vertically over the mixed layer from the ROMS-L2 model results. Right panels: same as the left panels, but integrated vertically from the surface down to 1200 m depth. The gray contours represent surface velocity magnitude > 0.5 m/s with intervals of 0.25 m/s.

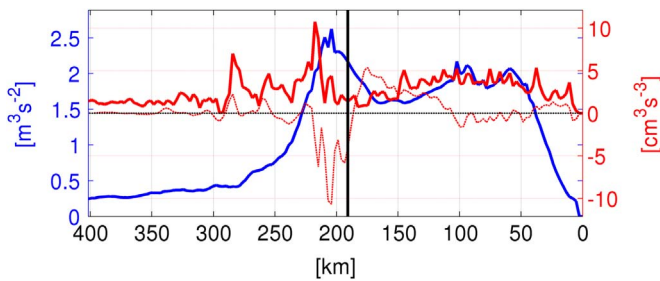


Fig. 8. Vertically integrated $K_m K_e$ (red thin line), $P_e K_e$ (red thick line) and K_e (blue line) over the mixed layer from ROMS-L2 along the transect shown by the black line in Fig. 5f. (For interpretation of the references to color in this figure legend, the reader is referred to the web version of this article.)

observations from the vertical section along the PN Line transect (e.g., Miyazawa et al., 2009), indicated by the thick black lines in Fig. 1. The PN Line measurements comprise 16 CTD (conductivity, temperature and depth) casts that have been obtained seasonally since 1972 by JMA research vessels. As this transect favorably transverses the Kuroshio path in the ECS, we can estimate the volume transport across the PN

Line. Comparisons of the seasonally averaged temperature and salinity clearly illustrate that the present model is capable of reproducing the observed stratification, not just in spring (Fig. 4) but in all seasons (not shown). A tilted thermocline and halocline are formed toward the ECS shelf region with subsurface salinity maxima in the trough region. Table 2 summarizes the modeled and observed volume flux (transport) in Sverdrup along the PN Line. The observed volume fluxes are estimated geostrophically from the slope of the isobaric surface, based on the seasonal climatology of the temperature and salinity (Fig. 4) by assuming the transport vanishes at 1000 m depth. The volume fluxes obtained by the models principally contain the ageostrophic component, which results in slightly larger transport than those observed. However, the modeled volume fluxes adequately capture the observed seasonal variability, such as the increase in summer and the decrease in fall. Interestingly, the ROMS-L2, with the finest grid resolution without TS nudging, provides a better estimate of the transport (compared with the observations) than that evaluated using the coarser-resolution models (viz., ROMS-L1 and JCOPE2), both of which employ data assimilation to some extent. This is likely attributable to the occurrence of an appropriate spontaneous flux adjustment in the ROMS-L2 through submesoscale lateral mixing and associated dissipation at

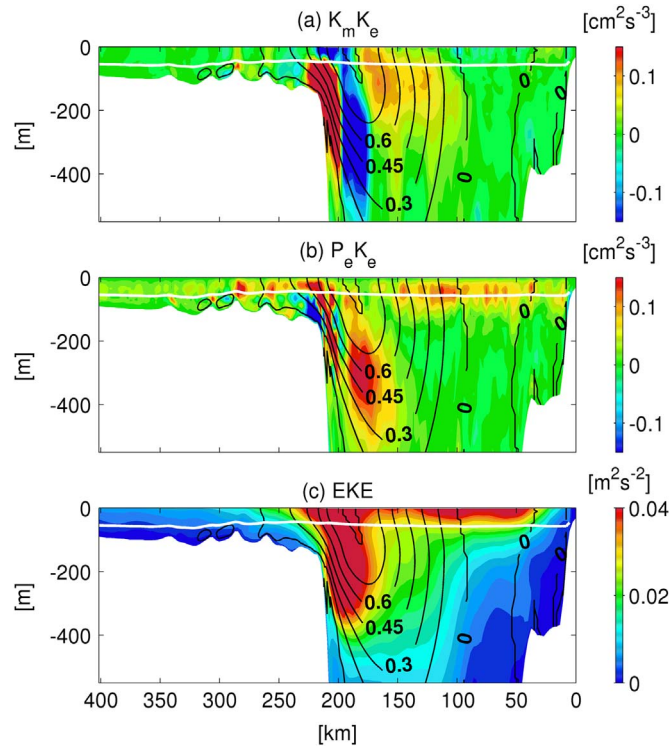


Fig. 9. Cross-sectional plots of: (a) barotropic conversion rate, $K_m K_e$, (b) baroclinic conversion rate, $P_e K_e$, and (c) EKE , K_e , from the ROMS-L2 model. The corresponding transect is shown by the black line in Fig. 5f. The white lines are the mean mixed-layer depth estimated from the KPP model in ROMS. The black contours represent the mean streamwise velocity normal to the transect.

the resolved scales of the mean KE around the Kuroshio path. In summary, the presented double-nested ROMS model is shown satisfactorily capable of reproducing the mesoscale behavior of the Kuroshio and the mean 3-D oceanic structure.

4. Downscaling effects

The unassimilated L2 model is capable of fully resolving submesoscale eddies, whereas the L1 and JCOPE2 are submesoscale-permitting (Capet et al., 2008a, 2008b, 2008c). Therefore, eddy activity should be enhanced by the grid refinement of the downscaling via the increase and strengthening of the resolved eddies. To examine the downscaling effects, surface eddy kinetic energy (EKE), K_e , can be estimated as follows:

$$K_e = \frac{1}{2} \left(\overline{u'^2 + v'^2} \right), \quad (1)$$

where (u, v) is the horizontal velocity and the overbar represents an ensemble-averaging operator. The overbars denote an ensemble-averaging operator. The variables assigned with the prime are the fluctuating eddy components obtained by removing the seasonal variations with a low-pass Butterworth filter in the frequency domain (the first and last 10% of the analysis period cannot be used because of the Butterworth filter's properties). Fig. 5a–c demonstrates that the surface EKE increases markedly as the model grid spacing decreases from 10 to 3 and to 1 km. The higher EKE mostly emerges in two distinct regions: one is on the Kuroshio axis and the other is on its eastern side, close to Okinawa (Main) Island.

Fig. 5d–f illustrates the daily averaged, surface relative vorticity normalized by the background rotation f (the Coriolis parameter), *viz.*, representing the emergence of mesoscale and submesoscale eddies in each model. The variable ζ/f is also known as the vortical Rossby number, the absolute value of which is greater than unity when

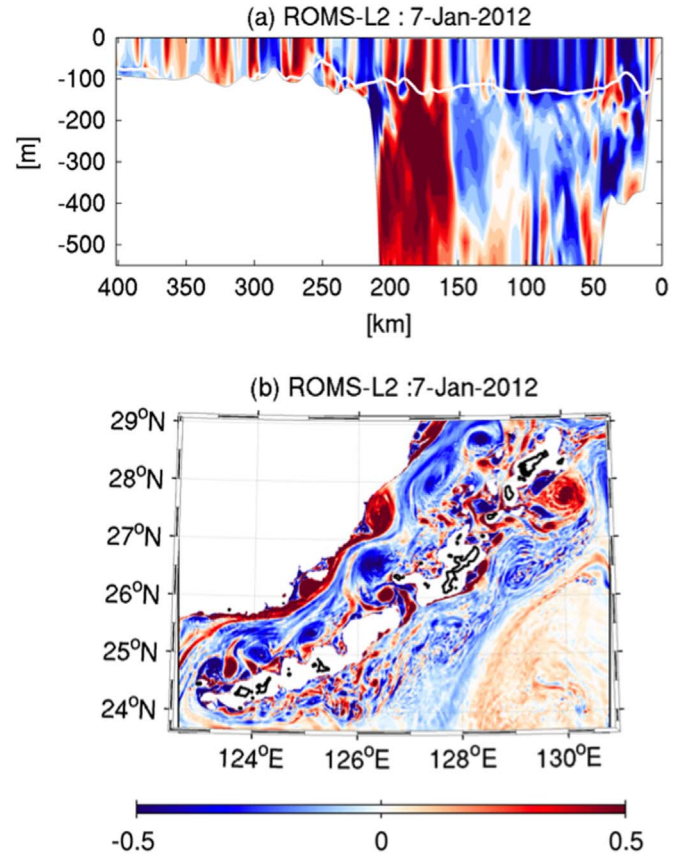


Fig. 10. (a) Cross-sectional plot of normalized relative vorticity ζ/f on January 7, 2012, along transect AA' (shown by the black line in Fig. 5f). The white line is the mixed-layer depth estimated from the KPP model. (b) Normalized relative vorticity ζ/f in the horizontal plane at $z = -400$ m on January 7, 2012.

ageostrophy is more evident. Vorticity is generally distributed as streaks and filaments around the Kuroshio axis where the change of sign occurs. However, enclosed circular eddies are dominant away from the axis, in particular, in the two ROMS model results. The two distinctive high EKE (K_e) regions in Fig. 5a–c are consistent with these vorticity distributions. As the resolution becomes finer, the extent and magnitudes of the resolved vortices become prominently diversified and enhanced, coinciding with the high EKE region on the eastern side of the Kuroshio (Fig. 5a–c). The higher-resolution model renders smaller submesoscale eddies that typically have diameters of several kilometers.

We notice that negative vorticity, *viz.*, counter-clockwise-rotating cyclonic eddies, develops more vigorously and widely on the east side of the Kuroshio than on the other side, where positive vorticity dominates. The innermost model with the highest resolution (ROMS-L2) captures the negative vorticity that is retained significantly on the eastern side of the Kuroshio, while the centrifugally stable positive vorticity is attenuated rather quickly there. The ROMS-L2 model has the smallest eddies and the largest negative vorticity near the islands. This negative bias near the islands, in the direction transverse to the Kuroshio path, is presumably caused by the increase of the resolved eddies with the increased model resolution. To confirm this negative bias quantitatively, the probability density function (PDF) of the normalized relative vorticity (ζ/f) at the surface was determined as a function of the westward transverse distance from Okinawa Island along transect AA', as shown in Fig. 5f. This transect is defined normal to the mean Kuroshio axis, averaged over the computational period, which is inclined at 35° relative to the geographical coordinate. Fig. 6 indicates that the finer-resolution models yield stronger vortices with gentler PDF slopes along the ordinates. Although the PDFs are

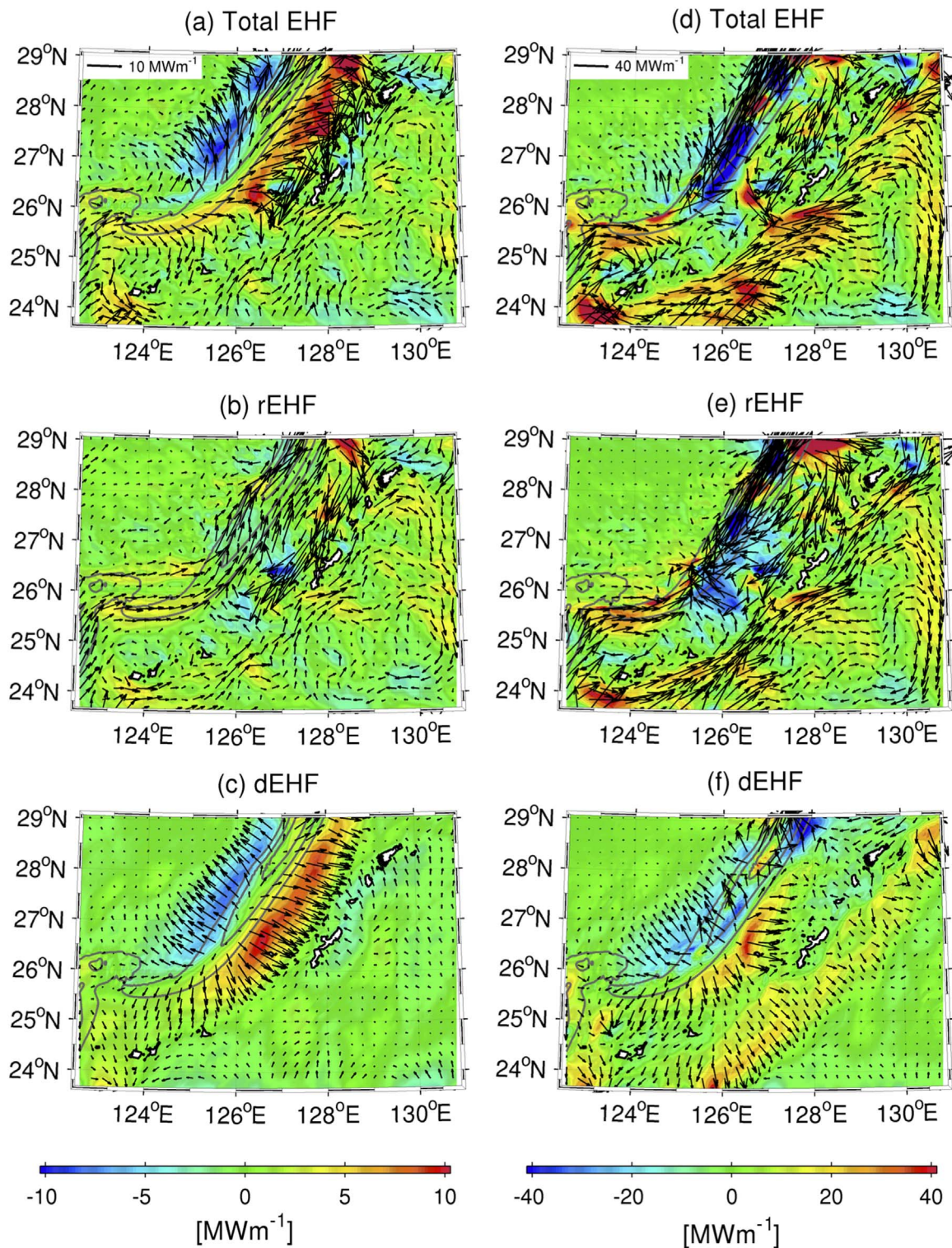


Fig. 11. Eddy heat flux (EHF) vectors vertically integrated (left) over the mixed layer and (right) from the surface to depth of 1200 m, superposed on the across-Kuroshio component of the labeled EHF (in color). (upper) total EHF, (middle) rotational component, rEHF, and (lower) divergent component, dEHF. The gray contours are surface velocity magnitude > 0.5 m/s with intervals of 0.25 m/s.

distributed nearly symmetrically with respect to the Kuroshio axis, they peak at $\zeta/f < 0$ on the eastern side of the Kuroshio axis, even adjacent to Okinawa Island. This negative bias on the east is most evident at the highest resolution. On the west of the Kuroshio, large positive vorticity appears immediately next to the Kuroshio, while the PDF peaks converge to zero away from the axis to the west. In summary, the Ryukyu Islands are considered to enhance both intensity and fluctua-

tions of the anticyclonic negative vorticity on the eastern side of the Kuroshio axis. However, on the other side, anticyclones and cyclones compete with the activated positive vorticity near the Kuroshio axis. This transverse asymmetry is a unique structure that characterizes the eddy field of the study area, which is perhaps related to both the topographic ridge near the island chain and the continental shelf break along which the Kuroshio persistently drifts (Fig. 1), as well as frontal

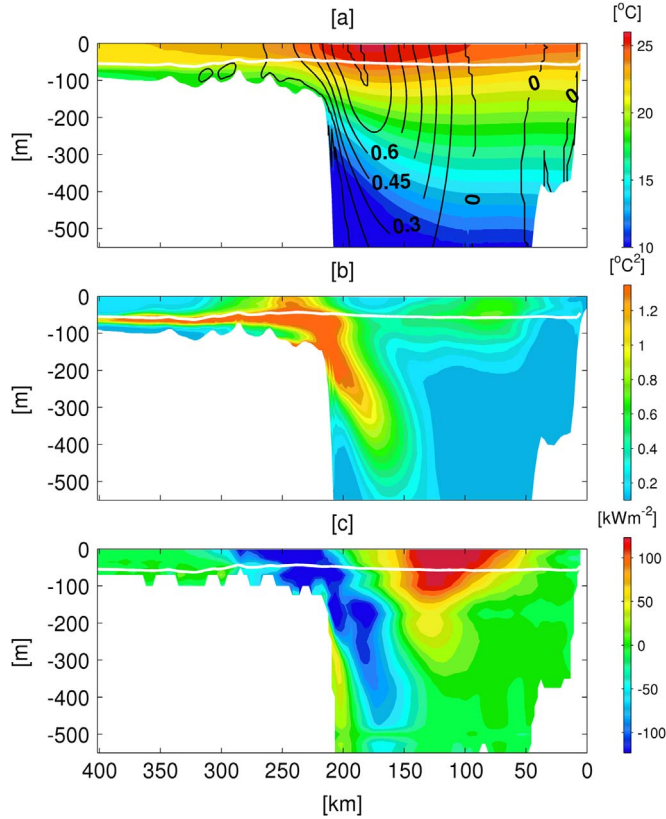


Fig. 12. Cross-sectional plots of: (a) mean streamwise velocity normal to the transect (contours) and mean temperature (color), (b) temperature variance, and (c) across-Kuroshio component of the divergent eddy heat flux, dEHF (eastward positive toward the islands) from the ROMS-L2 results, along the transect shown by the black line in Fig. 5f. White line shows the mean mixed-layer depth estimated from the KPP model.

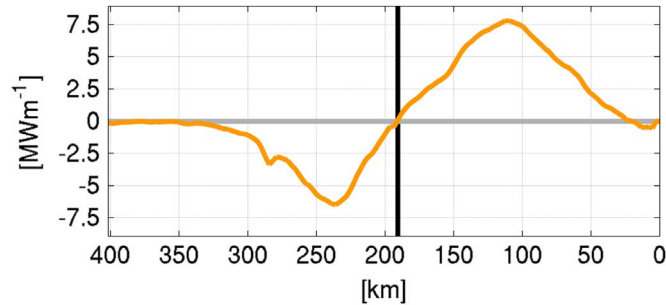


Fig. 13. Vertically integrated dEHF (eastward positive toward the islands) over the mixed layer from ROMS-L2 along transect AA' (as shown in Fig. 5f). The black line indicates the mean position of the Kuroshio axis.

processes associated with the Kuroshio warm water.

5. Energy conversion analysis

Energy conversion rates in the eddy kinetic energy (K_e) conservation equation are often used to quantify the relative importance of instability and eddy-mean interaction mechanisms (e.g., Marchesiello et al., 2003; Dong et al., 2006; Klein et al., 2008). If the conversion of mean kinetic energy to eddy kinetic energy $K_m K_e$ (viz., barotropic conversion rate) is positive, it implicates the occurrence of shear instability in the extraction of K_e to energize eddies. If the conversion of eddy potential energy to eddy kinetic energy $P_e K_e$ (viz., baroclinic conversion rate) is positive, baroclinic instability is expected. We focus on these two primary quantities, as expressed in the following equations, in the investigation of the stimulation mechanisms of K_e :

$$K_m K_e = - \left(\overline{u'u'} \frac{\partial \bar{u}}{\partial x} + \overline{u'v'} \frac{\partial \bar{u}}{\partial y} + \overline{u'w'} \frac{\partial \bar{u}}{\partial z} + \overline{v'u'} \frac{\partial \bar{v}}{\partial x} + \overline{v'v'} \frac{\partial \bar{v}}{\partial y} + \overline{v'w'} \frac{\partial \bar{v}}{\partial z} \right), \quad (2)$$

$$P_e K_e = - \frac{g}{\rho_0} \overline{\rho' w'}, \quad (3)$$

where (x, y, z) are the horizontal and vertical coordinates, w is the vertical velocity, ρ is the density of sea water, $\rho_0 = 1027.5 \text{ kg m}^{-3}$ is the Boussinesq reference density, and g is gravitational acceleration. The vertically integrated $K_m K_e$, $P_e K_e$, and K_e (EKE) over the mixed layer from the ROMS-L2 model are plotted in Fig. 7a–c. The averaged mixed-layer depth estimated by the KPP model (Large et al., 1994) used in the ROMS is approximately 50 m in the L2 domain. The mixed-layer integrated $P_e K_e$ is positive almost everywhere with two distinctly high regions around the Kuroshio axis and the neighboring flank on the eastern side to the islands (Fig. 7b). This $P_e K_e$ distribution illustrates the importance of baroclinic instability in the vorticity generation within these two regions. In contrast, an axisymmetric pair of large positive and negative areas of $K_m K_e$ can be observed in the narrow strips on both sides of the Kuroshio, representing the lateral shear instability induced by the Kuroshio (Fig. 7a). In general, the regions with positive $P_e K_e$ and positive $K_m K_e$ coincide with the areas of high K_e (Fig. 7c).

The area of highly positive $P_e K_e$ is distributed widely between the Kuroshio path and the Ryukyu Islands, whereas the highly positive $K_m K_e$ appears mostly near the Kuroshio and on the western side of the islands near the topography. The vertically integrations of $K_m K_e$, $P_e K_e$, and K_e over the mixed layer along the transect are plotted in Fig. 8. Consistent with Fig. 7a–c, $P_e K_e$ is positive and larger than $K_m K_e$ almost everywhere along the transect, indicating that baroclinic instability is the dominant mechanism for eddy generation near the surface, especially, on the eastern side of the Kuroshio path where high values of K_e appear. Therefore, it is manifest that the negative vorticity on the eastern side of the Kuroshio (Fig. 5f) is provoked by a combination of the lateral shear affected by the Kuroshio, topographic eddy shedding near the islands, and baroclinic instability due to the Kuroshio front. The negative $K_m K_e$ on the western side of the Kuroshio suggests that positive vorticity is suppressed by the lateral shear through an inverse energy cascade while baroclinically destabilized by the competing positive $P_e K_e$.

The EKE (K_e) budget is examined further for the subsurface water, where the Kuroshio is influential, by vertical integration of $K_m K_e$, $P_e K_e$, and K_e from the surface down to a depth of 1200 m with the L2 result (Fig. 7d–f). The L2 model detects large positive barotropic and baroclinic conversion rates near the Kuroshio that coincide with the region of high K_e . In addition, an increase of the subsurface $P_e K_e$ and resultant intensification of K_e are evident on the eastern side of the islands, due to a branch of the Kuroshio known as the *Ryukyu (Under) Current* (e.g., Kawabe, 2001; Andres et al., 2008). This large $P_e K_e$ could induce further subsurface westward lateral mixing and intrusion of the Ryukyu Current. However, this is beyond the scope of the present study and it will be examined elsewhere. The subsurface structure on the western side of the islands is illustrated in Fig. 9 with respect to the vertical cross-section along transect AA' (see Fig. 5f). The Kuroshio main body is inclined on the shelf slope with a mean streamwise velocity of $> 0.2 \text{ m/s}$, even at 600 m depth. High K_e is distributed widely near the surface to the east, coinciding with the positive $K_m K_e$ near the Kuroshio and positive $P_e K_e$ extending between the Kuroshio and Okinawa Island. Conversely, high K_e is mostly confined along the shelf break from the surface to 400 m depth to the west, where both $K_m K_e$ and $P_e K_e$ increase in magnitude with the sign change.

Below the mixed layer, the Kuroshio is squeezed strongly against the shelf slope on the eastern side, which provokes large velocity shear and thus large positive $K_m K_e$, which is associated with the shear instability due to topographic eddy shedding. Around the inclined Kuroshio core, competing large positive $P_e K_e$ and large negative $K_m K_e$

are formed simultaneously below the mixed layer down to a depth of 600 m. Fig. 10 shows a snapshot of the daily averaged, normalized relative vorticity (ζ/f) field in the vertical section along the transect and in the horizontal section at $z=-400$ m from the L2 model. In Fig. 10a, negative vorticity (anticyclonic submesoscale eddies) appears dominantly near the surface on the eastern side of the Kuroshio toward Okinawa Island, while positive cyclonic vorticity appears around the Kuroshio core from the surface down to depths beyond 500 m along the shelf slope. The diameter of this cyclone is approximately 50 km, which still fits within a typical submesoscale range. In Fig. 10b, cyclonic eddy shedding occurs quasi-periodically from the shelf slope topography. Therefore, a combination of topographic shear and baroclinic instability promotes the near-surface anticyclonic eddies and subsurface cyclonic eddies, both of which are submesoscale.

6. Heat flux analysis

The submesoscale anticyclonic eddies induced by the Kuroshio are anticipated to promote eastward material transport to the west coast of Okinawa Island through lateral eddy mixing. To quantify this effect, we assessed the lateral turbulent mixing of a tracer (*i.e.*, heat) in the upper ocean. The time-averaged, vertically integrated heat (potential temperature) transport equation is represented as (*e.g.*, Marchesiello et al., 2003):

$$\int_{-h}^{\eta} \left(\frac{\partial \bar{\pi} \bar{T}}{\partial x} + \frac{\partial \bar{v} \bar{T}}{\partial y} \right) dz + \int_{-h}^{\eta} \left(\frac{\partial \bar{u} \bar{T}}{\partial x} + \frac{\partial \bar{v} \bar{T}}{\partial y} \right) dz + \int_{-h}^{\eta} [Q(\bar{T}) + D(\bar{T})] dz = 0, \quad (4)$$

where T is potential temperature, Q is the sea surface heat flux, D is the parameterized vertical and horizontal subgrid-scale mixing of heat, h is depth, and η is surface elevation. We focus on the advective transport by eddy flow, which is a divergence of lateral eddy heat fluxes (EHFs) \mathbf{F} :

$$\mathbf{F} = (F_x, F_y) = (\rho_0 C_p \bar{u} \bar{T}', \rho_0 C_p \bar{v} \bar{T}') \quad (5)$$

where $C_p = 4000 \text{ J kg}^{-1} \text{ } ^\circ\text{C}^{-1}$, which is the heat capacity of seawater at a constant pressure. To quantify the eddy heat transport to the islands, a divergent component of the EHF is evaluated. The EHF can be decomposed into divergent and rotational components using Helmholtz's theorem (*e.g.*, Aoki et al., 2013) such that

$$\mathbf{F} = \mathbf{k} \times \nabla \psi + \nabla \varphi \equiv \text{rEHF} + \text{dEHF}, \quad (6)$$

where \mathbf{k} is a vertical unit vector, and ψ and φ are scalar quantities similar to a streamfunction and a velocity potential, respectively. We introduce the notation where rEHF and dEHF are the rotational and divergent components of the EHF. This decomposition is conducted by numerically solving the Poisson Eq. (6) with Neumann boundary conditions.

The mixed-layer integrated EHF, rEHF, and dEHF vectors, superimposed on their transverse component relative to the mean Kuroshio path from the L2 result, are plotted in Fig. 11a–c. The total EHF (Fig. 11a) is properly decomposed into the rEHF (Fig. 11b) and dEHF (Fig. 11c). The rEHF vectors mainly follow the prevailing direction of the northeastward-drifting Kuroshio path with recurring southwestward eddy heat transport near the islands. The eddy heat transport in the opposite direction to the Kuroshio near the islands is obviously due to a mesoscale secondary circulation often known as the *Kuroshio Counter Current*, as reported in previous studies (*e.g.*, Qiu and Imasato, 1990). However, the mixed-layer integrated dEHF properly measures the contribution normal to the Kuroshio axis, which manifests the lateral eddy heat transport toward the islands. Fig. 11c also demonstrates that the near-surface heat transport to the islands occurs more strongly on the eastern side of the Kuroshio, although a weaker northwestward heat transport occurs on the other side. This near-surface heat transport toward the islands is obviously induced by

anticyclonic submesoscale eddies developed around the Ryukyu Islands (Section 4).

Fig. 11d–f shows the vertically integrated EHF vectors from the surface to 1200 m depth. In general, the vectors are similar to those integrated over the mixed layer, although several substantial differences can be observed. The total EHF and rEHF occurs mainly in the direction of the Kuroshio path, whereas the major transport bifurcates around Ishigaki Island, which is located near the lower-left corner of the domain, forming the Ryukyu Current EHF branch that passes on the eastern side of Okinawa Island. As this subsurface branch drifts close to several islands, including Okinawa Island, the influence of the Kuroshio on the Ryukyu Islands is partially brought by this under current. Other differences include the attenuated positive across-Kuroshio transport (dEHF) between the Kuroshio and Okinawa Island and the southeastward subsurface dEHF on the eastern side of the islands due to the Ryukyu Current. These findings illustrate that the near-surface dEHF brings the Kuroshio warm water to the islands, whereas the subsurface dEHF affects them in a different way.

Fig. 12 shows cross-sectional plots of mean temperature, temperature variance, and dEHF (eastward positive to Okinawa Island) along the transect. The mean thermocline and mixed-layer depths become shallower toward the ECS shelf from Okinawa Island. However, the Kuroshio induces additional effects such that the mean thermocline is inclined to shallow both toward the ECS shelf and toward Okinawa Island, with a near-surface bulge of warm water around the Kuroshio axis.

The maximum lateral temperature gradient is formed adjacent to the Kuroshio core that is inclined on the shelf slope. The overall stratification is increased by this inclined thermocline, established from the thermal wind relation with the cross-sectional velocity structure due to the Kuroshio. Although the across-Kuroshio dEHF is positive and confined mostly in the mixed layer in the east, a tongue of negative dEHF is formed in the west, which penetrates to a depth of 400 m along the slope (Fig. 12c). The temperature variance (Fig. 12b) is large where the dEHF and K_e (see Fig. 8c) are consistently large. Interestingly, the temperature variance is increased around the mean mixed-layer depth on the ECS shelf, perhaps provoked by temporal fluctuations of the thermocline.

The mixed-layer integrated dEHF along the transect (Fig. 13) indicates that energetic lateral eddy heat transport is induced within and around the surface mixed layer, leading to the zonal transport of the Kuroshio warm water. The positive eddy flux develops more strongly on the eastern side of Kuroshio than does the negative flux on the other side in the mixed layer. Nevertheless, the largest temperature variance emerges between the Kuroshio and the slope where the tongue of negative dEHF exists. The subsurface topographic eddy shedding on the slope (Fig. 10) promotes this tongue of negative dEHF, which results in subsurface westward heat transport via the warm water brought up from the bottom of the Kuroshio to the ECS shelf. As a consequence of all these processes, lateral eddy heat transport occurs asymmetrically relative to the Kuroshio path.

7. Conclusions

Eddy-induced lateral mixing due to the Kuroshio around the Ryukyu Islands in the ECS was investigated using a double-nested ROMS model that downscales the assimilative JCOPE2 oceanic reanalysis to the innermost submesoscale eddy-resolving model with 1-km grid spacing. An extensive model-data comparison was performed against field observations and satellite altimetry data to demonstrate the model's capability of reproducing the Kuroshio and 3-D oceanic structure. The model-data comparison demonstrated that the elaborated innermost high-resolution ROMS-L2 model successfully reproduced mesoscale structures spontaneously without any data assimilation.

The L2 models simulated significant negative vorticity bias, com-

prising anticyclonic mesoscale and submesoscale eddies, on the western side of the islands. The PDF of the normalized relative vorticity along the transect normal to the mean Kuroshio path supported this asymmetric appearance of negative vorticity. Positive vorticity was confined mostly to the vicinity of the Kuroshio, while the peak vorticity PDF converged to zero (*viz.*, almost no positive and negative bias) toward the ECS shelf. These results reinforce the speculation that eddies are generated because of interactions between the Kuroshio warm water and the unique local topography, including the ridge of the islands to the east and the ECS continental shelf break to the west, along which the Kuroshio persistently flows.

The energy conversion analysis focusing on the barotropic and baroclinic conversion rates suggested that the near-surface anticyclonic negative vorticity on the eastern side of the Kuroshio and the subsurface cyclonic positive vorticity on the western side are generated via the combination of shear instability and baroclinic instability, both of which are evidently influenced by the Kuroshio. Conversely, the negative barotropic conversion rate, which appeared near the Kuroshio axis, suggested that cyclonic positive vorticity is suppressed by the Kuroshio's lateral shear near the surface. The resultant surface EKE is thus also asymmetric with respect to the Kuroshio, with greater EKE distributed widely on the eastern side of the path. However, the subsurface water below the mixed layer reflected a pronouncedly different energy balance. The magnitude of the subsurface barotropic conversion rate is large on the shelf break, where a positive conversion rate appears near the slope, whereas a negative rate appears to the east, where it competes with a large positive baroclinic conversion rate.

The heat flux analysis solidly explained that these eddies promote lateral material transport from the Kuroshio. Helmholtz decomposition was introduced to the EHF, rEHF, and dEHF. The decomposed rEHF detected the contribution from the EHF that mainly follow the Kuroshio and the anticyclonic recurring secondary circulation referred to as the *Kuroshio Counter Current*. Conversely, the dEHF measured the contribution normal to the Kuroshio axis, which represents the transverse eddy-induced transport to the islands. The surface lateral eddy heat transport occurs asymmetrically relative to the Kuroshio axis, with greater transverse eastward transport than toward the ECS shelf. This occurs because of the more energetic anticyclonic submesoscale eddies on the eastern side of the Kuroshio. Consistent with the subsurface energy conversion rates, the depth-integrated EHF, rEHF, and dEHF occur mainly in the direction of the Kuroshio path, the across-Kuroshio transport (*viz.*, dEHF) showed that they can be enhanced significantly near the surface, which promotes warm water transport in both transverse directions relative to the Kuroshio path. However, a “negative dEHF tongue” was found to form uniquely on the shelf slope and thus the subsurface warm water is brought upward along the slope toward the ECS shelf. This negative dEHF tongue was attributed to subsurface eddies generated by a combination of the baroclinic and shear instability, according to the energy conversion analysis. These subsurface eddies are evidently shed on the ECS shelf slope down to a depth of 600 m as energetic cyclonic submesoscale eddies.

The present study clarified that the Kuroshio warm water undoubtedly influences the biologically diverse ecosystems with abundant corals that have formed around the Ryukyu Islands through mechanical intrusion. Based on the modeling results, it was established that the Kuroshio-derived waters approach the islands in at least three ways: 1) by transverse eddy-induced lateral mixing near the surface, 2) via a clockwise recurring flow known as the *Kuroshio Counter Current*, and 3) via a subsurface pathway associated with the *Ryukyu Current*. This study focused primarily on the first mechanism that is accompanied by subsurface submesoscale eddy transport toward the ECS shelf, induced by topographic eddy shedding on the slope. Further analysis will be required to elucidate the detailed mechanisms leading to the other two processes.

Acknowledgements

We are grateful to James C. McWilliams, Alexander F. Shchepetkin, and M. Jeroen Molemaker of UCLA and Mayumasa Miyazawa of JAMSTEC for their help and comments on the numerical modeling. We are also grateful to Shohei Nakada of OIST for his help on the organizing JMA's research vessels data. This study was supported by JSPS Grant-in-Aid for Scientific Research C and B (KAKENHI grant numbers: 24560622 and 15H04049).

References

- Andres, M., Park, J., Wimbush, M., Zhu, X., Chang, K., Ichikawa, H., 2008. Study of the Kuroshio/Ryukyu current system based on satellite-altimeter and in situ measurements. *J. Oceanogr.* 64, 937–950.
- Aoki, K., Minobe, S., Tanimoto, Y., Sasai, Y., 2013. Southward eddy heat transport occurring along southern flanks of the Kuroshio extension and the gulf stream in a 1/108 global ocean general circulation model. *J. Phys. Oceanogr.* 43, 1899–1910.
- Badin, G., Tandon, A., Mahadevan, A., 2011. Lateral mixing in the pycnocline by baroclinic mixed layer eddies. *J. Phys. Oceanogr.* 41, 2080–2101.
- Becker, J.J., Sandwell, D.T., Smith, W.H.F., Braud, J., Binder, B., Depner, J., Fabre, D., Factor, J., Ingalls, S., Kim, S.-H., Ladner, R., Marks, K., Nelson, S., Pharaoh, A., Trimmer, R., Von Rosenberg, J., Wallace, G., Weatherall, P., 2009. Global bathymetry and elevation data at 30" resolution: SRTM30_PLUS. *Mar. Geod.* 32 (4), 355–371.
- Bentamy, A., Ayina, H.-L., Queffelecoul, P., Croize-Fillon, D., 2006. Improved near real time surface wind resolution over the Mediterranean Sea. *Ocean Sci. Discuss.* 3 (3), 435–470.
- Blumberg, A.F., Mellor, G.L., 1987. A description of a three-dimensional coastal ocean circulation model. In: Heaps, N. (Ed.), *Three-Dimensional Coastal Ocean Models*. Coastal and estuarine Sciences. Amer. Geophys. Union, Washington, D.C., USA, 1–16.
- Boccaletti, G., Ferrari, R., Fox-Kemper, B., 2007. Mixed layer instabilities and restratification. *J. Phys. Oceanogr.* 37, 2228–2250.
- Callies, J., Ferrari, R., Klymak, J.M., Gula, J., 2015. Seasonality in submesoscale turbulence. *Nat. Commun.* 6, Article number: 6862.
- Capet, X., McWilliams, J.C., Molemaker, J.M., Shchepetkin, A.F., 2008a. Mesoscale to submesoscale transition in the California current system. Part I: flow structure, eddy flux, and observational tests. *J. Phys. Oceanogr.* 38, 29–43.
- Capet, X., McWilliams, J.C., Molemaker, J.M., Shchepetkin, A.F., 2008a. Mesoscale to submesoscale transition in the California current system. Part II: frontal processes. *J. Phys. Oceanogr.* 38, 44–64.
- Capet, X., McWilliams, J.C., Molemaker, J.M., Shchepetkin, A.F., 2008b. Mesoscale to submesoscale transition in the California current system. Part III: energy balance and flux. *J. Phys. Oceanogr.* 38, 2256–2269.
- Cesar, H.J.S., Burke, L., Pet-Soede, L., 2003. *The Economics of Worldwide Coral Reef Degradation*. Cesar Environmental Economics Consulting, Arnhem, and WWF-Netherlands, Zeist, The Netherlands. 23pp.
- Centurioni, L.R., Niiler, P.P., Lee, D.K., 2004. Observations of inflow of Philippine sea surface water into the South China Sea through the Luzon Strait. *J. Phys. Oceanogr.* 34, 113–121.
- Dai, A., Qian, T., Trenberth, K.E., Milliman, J.D., 2009. Changes in continental freshwater discharge from 1948–2004. *J. Clim.* 22, 2773–2791.
- Dong, C., McWilliams, J.C., Shchepetkin, A.F., 2006. Island wakes in deep water. *J. Phys. Oceanogr.* 37, 962–981.
- Dong, C., McWilliams, J.C., 2007. A numerical study of island wakes in the Southern California bight. *Cont. Shelf Res.* 27, 1233–1248.
- Gula, J., Molemaker, M.J., McWilliams, J.C., 2014. Submesoscale cold filaments in the Gulf Stream. *J. Phys. Oceanogr.* 44, 2617–2643.
- Guo, X., Hukuda, H., Miyazawa, Y., Yamagata, T., 2003. A triply nested ocean model for simulating the Kuroshio—roles of horizontal resolution on JEBAR. *J. Phys. Oceanogr.* 33, 146–169.
- Ichikawa, H., Beardsley, R.C., 1993. Temporal and spatial variability of volume transport of the Kuroshio in the East China Sea. *Deep-Sea Res.* 40, 583–605.
- Ichikawa, H., Chaen, M., 2000. Seasonal variation of heat and freshwater transports by the Kuroshio in the East China Sea. *J. Mar. Syst.* 24, 119–129.
- Imawaki, S., Uchida, H., Ichikawa, H., Fukazawa, M., Umatani, S., the ASUKA Group, 2001. Satellite altimeter monitoring the Kuroshio transport south of Japan. *Geophys. Res. Lett.* 28 (1), 17–20.
- Isoguchi, O., Shimada, M., Kawamura, H., 2010. Characteristics of ocean surface winds in the lee of an isolated island observed by synthetic aperture radar. *Mon. Weather Rev.* 139, 1744–1761.
- Johns, W.E., Lee, T.N., Zhang, D., Zantopp, R., 2001. The Kuroshio East of Taiwan: Moored transport observations from the WOCE PCM-1 array. *J. Phys. Oceanogr.* 31, 1031–1053.
- Kawabe, M., 2001. Interannual variations of sea level at Nansei Islands and volume transport of the Kuroshio due to wind changes. *J. Phys. Oceanogr.* 31, 189–205.
- Klein, P., Hua, B.-L., Lapeyre, G., Capet, X., Le Gentil, S., Sasaki, H., 2008. Upper ocean turbulence from high-resolution 3D simulations. *J. Phys. Oceanogr.* 38, 1748–1763.
- Kunze, E., Klymak, J.M., Lien, R.-C., Ferrari, R., Lee, C.M., Sundermeyer, M.A., Goodman, L., 2015. Submesoscale water-mass spectra in the Sargasso Sea. *J. Phys. Oceanogr.* 45, 1325–1338.

- Large, W.G., McWilliams, J.C., Doney, S.C., 1994. Oceanic vertical mixing: a review and model with a nonlocal boundary layer parameterization. *Rev. Geophys.* 32, 363–403.
- Marchesiello, P., McWilliams, J.C., Shchepetkin, A., 2003. Equilibrium structure and dynamics of the California current system. *J. Phys. Oceanogr.* 33, 753–783.
- Mason, E., Molemaker, J., Shchepetkin, A.F., Colas, F., McWilliams, J.C., Sangrà, P., 2010. Procedures for offline grid nesting in regional ocean models. *Ocean Model.* 35, 1–15.
- Miyazawa, Y., Guo, X., Yamagata, T., 2004. Roles of mesoscale eddies in the Kuroshio paths. *J. Phys. Oceanogr.* 34, 2203–2222.
- Miyazawa, Y., Zhang, R., Guo, X., Tamura, H., Ambe, D., Lee, J., Okuno, A., Yoshinari, H., Setou, T., Komatsu, K., 2009. Water mass variability in the Western North Pacific detected in 15-year eddy resolving ocean reanalysis. *J. Oceanogr.* 65, 737–756.
- Nadaoka, K., Nihei, Y., Wakaki, K., Kumano, R., Kakuma, S., Moromizato, S., Omija, T., Iwao, K., Shimike, K., Taniguchi, H., Nakano, Y., Ikema, T., 2001. Regional variation of water temperature around Okinawa coasts and its relationship to offshore thermal environments and coral bleaching. *Coral Reefs* 20, 373–384.
- Nakamura, H., Nonaka, M., Sasaki, H., 2009. Seasonality of the Kuroshio path destabilization phenomenon in the Okinawa Trough: a numerical study of its mechanism. *J. Phys. Oceanogr.* 40, 530–550.
- Penven, P., Debreu, L., Marchesiello, P., McWilliams, J.C., 2006. Evaluation and application of the ROMS 1-way embedding procedure to the California current upwelling system. *Ocean Model.* 12, 157–187.
- Qiu, B., Imasato, N., 1990. A numerical study on the formation of the Kuroshio counter current and the Kuroshio branch current in the East China Sea. *Cont. Shelf Res.* 10, 165–184.
- Qiu, B., 2001. Kuroshio and Oyashio Currents. In: *Encyclopedia of Ocean Sciences*. Academic Press, pp. 1413–1425.
- Roads, J., 2004. Experimental weekly to seasonal U.S. forecasts with the regional spectral model. *Bull. Am. Meteor. Soc.* 85, 1887–1902.
- Rodriguez, E., Morris, C.S., Belz, J.E., Chapin, E.C., Martin, J.M., Daffer, W., Hensley, S., 2005. An Assessment of the SRTM Topographic Products. Jet Propulsion Laboratory, Pasadena, California, 143.
- Romero, L., Uchiyama, Y., Ohlman, J.C., McWilliams, J.C., Siegel, D.A., 2013. Simulations of nearshore particle-pair dispersion in Southern California. *J. Phys. Oceanogr.* 443, 1862–1879.
- Sasaki, H., Klein, P., Qiu, B., Sasai, Y., 2014. Impact of oceanic-scale interactions on the seasonal modulation of ocean dynamics by the atmosphere. *Nat. Commun.* 5, Article number: 5636.
- Sasaki, Y., Minobe, S., Inatsu, M., 2012. Influence of the Kuroshio in the East China Sea on the early summer (Baiu) rain. *J. Clim.* 25, 6627–6645.
- Shchepetkin, A.F., McWilliams, J.C., 2005. The regional ocean modeling system (ROMS): a split-explicit, free-surface, topography-following-coordinate oceanic model. *Ocean Model.* 9, 347–404.
- Shchepetkin, A.F., McWilliams, J.C., 2008. Computational kernel algorithms for fine-scale, multiprocess, longtime oceanic simulations. In: Temam, R., Tribbia, J. (Eds.), *Handbook of Numerical Analysis*. Elsevier, Amsterdam, 119–181.
- Spalding, M.D., Ravilious, C., Green, E.P., 2001. *World Atlas of Coral Reefs*. The UNEP-World Conservation Monitoring Centre, University Of California Press, Berkeley, USA, 432.
- Traon, P.Y.L., Nadal, F., Ducet, N., 1998. An improved mapping method of multisatellite altimeter data. *J. Atmos. Ocean. Technol.* 15, 522–534.
- Uchiyama, Y., Idica, E.Y., McWilliams, J.C., Stolzenbach, K.D., 2014. Wastewater effluent dispersal in Southern California Bays. *Cont. Shelf Res.* 76, 36–52.
- Usui, N., Ishizaki, S., Fujii, Y., Tsujino, H., Yasuda, T., Kamachi, M., 2006. Meteorological Research Institute Multivariate Ocean Variational Estimation (MOVE) system: some early results. *Adv. Space Res.* 37, 806–822.
- Usui, N., Tsujino, H., Fujii, Y., Kamachi, M., 2008. Generation of a trigger meander for the 2004 Kuroshio large meander. *J. Geophys. Res.* 113, C01012.
- Woodruff, S.D., Slutz, R.J., Jenne, R.L., Steurer, P.M., 1987. A comprehensive ocean-atmosphere data set. *Bull. Am. Meteor. Soc.* 68, 1239–1250.
- Xu, H., Xu, M., Xie, S., Wang, Y., 2011. Deep atmospheric response to the spring Kuroshio current over the East China Sea. *J. Clim.* 24, 4959–4972.
- Yang, D., Yin, B., Liu, Z., Feng, X., 2011. Numerical study of the ocean circulation on the East China Sea shelf and a Kuroshio bottom branch northeast of Taiwan in summer. *J. Geophys. Res.* 116, C05015.